

CRLS: Convolutional Regularized Least Squares Framework for Reduced Order Modeling of Transonic Flows

Muhammad Bilal ^{*1} and Ashwin Renganathan^{†2}

¹Penn State

²Virginia Tech

Abstract

We develop a convolutional regularized least squares (**CRLS**) framework for reduced-order modeling of transonic flows with shocks. Conventional proper orthogonal decomposition (POD)-based reduced models are attractive because of their optimality and low online cost; however, but they perform poorly when snapshots contain parameter-dependent discontinuities, leading to smeared shocks, stair-stepping, or non-physical oscillations. In **CRLS**, we first map each full-order snapshot to a smoother representation by applying a one-dimensional Gaussian convolution with reflect padding along the flow field coordinates. The convolution hyperparameters (kernel width and support) are selected automatically by Bayesian optimization on a held-out set of snapshots. POD bases are then extracted from the smoothed data, and the parametric dependence of the POD coefficients is learned via radial basis function interpolation. To recover sharp shock structures, we introduce an efficient deconvolution step formulated as a regularized least squares problem, where the regularization centers the reconstruction around a nearest-neighbor reference snapshot in parameter space. The resulting **CRLS** surrogate is evaluated on inviscid transonic flow over the RAE2822 airfoil, modeled by the steady compressible Euler equations solved with SU2 over a Latin-hypercube sample of Mach number and angle of attack. Compared with standard POD and smoothed-POD baselines, **CRLS** yields markedly improved shock location and strength, lower surface-pressure and field-level errors, and a 42% reduction in the number of POD modes required to capture a fixed fraction of snapshot energy. These results demonstrate that **CRLS** provides an accurate, data-efficient, and largely automated route to shock-aware reduced-order models for high-speed aerodynamic design.

^{*}Graduate student, Kevin T. Crofton Department of Aerospace and Ocean Engineering.

[†]Assistant professor, Aerospace Engineering and the Institute of Computational and Data Science (ICDS).

1 Introduction

In aircraft design, full-scale numerical simulations of aerodynamic fluid flows, particularly flows involving phenomena like shock waves, require extensive computational resources and run times. With the revival of interest in commercial supersonic transportation, the need for accurately capturing the parametric variation of shock strength and location has been unprecedented. While advances in numerical methods, e.g., with shock capturing schemes [36, 42, 40, 17, 4, 13], have enabled this, they are still prohibitive to be used in a design setting where they will have to be queried many times. Emulating such flows with a computationally cheap surrogate model would be more appropriate for a design setting; however, that introduces a unique set of challenges that must still be addressed. This work aims to address the challenges involved in accurately emulating shock-dominated flows with a surrogate model.

Reduced order modeling (ROM) [39] approximates the state of a system of partial differential equations (PDEs) in terms of a finite number of “basis” solutions. If the basis solutions are well chosen, then this offers an effective way to reduce the number of degrees of freedom in the PDE system, thereby offering a computationally cheap surrogate model. At the core of most ROMs are the methods for determining a suitable reduced basis. Approaches such as proper orthogonal decomposition (POD) [1, 35], dynamic mode decomposition (DMD) [38] for unsteady flows, balanced POD [34], deep neural autoencoders [23, 21, 14], and Fourier neural operators (FNO) [19, 5], offer powerful tools for identifying the most dominant flow structures in the full order model (FOM). By capturing the key features of the underlying system with a handful of dominant modes, these methods preserve the essential physics of fluid flow while significantly reducing the computational cost.

Among all the reduced basis methods, POD based methods are particularly attractive. This is because (i) the POD bases are *optimal* [1] in the sense that they represent the best choice of basis solutions that capture the dominant energy modes in the flow, and (ii) they offer a linear mapping between the reduced and full order solution, making computation simple; we provide a formal introduction to POD in section 1.1. However, POD-based ROM methods face challenges when dealing with convection-dominated and multi-scale flows [29, 27, 28, 22, 45]. There are two perspectives as to why this is true. First, convection-dominated and multiscale flows are endowed with a wide spectrum of scales; POD, which is based on the singular value decomposition (SVD), is ideal when larger integral scales of the flow dominate. Second, a simple linear combination of a basis set might not be adequate to capture sharp gradients; for instance, a linear combination of two step functions cannot lead to another step function for non-zero weights; we provide an illustration in section 1.2. Shocks are an example of sharp changes in flow features. Projection-based ROMs typically depend on the smooth low-dimensional modal expansions, and these expansions struggle to capture sharp changes without smearing or introducing non-physical oscillations (similar to the Gibbs phenomenon [15]).

Researchers gravitate towards POD because of its low computational cost, theoretical soundness, and the ability to handle large data sets. But it struggles to capture strong nonlinear effects, like shock waves. Several works exist that address the aforementioned shortcomings of POD-based ROMs for shock-dominated flows. Examples include adaptive h-refinement [3] which adaptively refines reduced-order models a posteriori on the inviscid

Burgers equations, projection-based ROM using a Koopman-based approach for high subsonic and transonic flows [28, 33], transported snapshot model order reduction [22] which works by transporting the snapshots to the desired location and solving the minimization problem, combining POD with DMD [46] to construct an evolution model for POD mode coefficients which uses DMD with specific control to predict unsteady transonic flow. Most of these POD-based ROM models have traditionally treated high-order systems as if they were linear. But transonic aerodynamic flows with strong nonlinear features such as shocks are discontinuous in nature as well. This makes it hard to accurately predict the flow features using POD without manipulating the data to remove these discontinuities.

Recently, researchers are more focused on developing data-driven flow models based on deep learning techniques to predict the flow behaviour for highly non-linear systems [18], [2], [48]. The combination of complex network architectures and advanced algorithms to train them offer tremendous potential. This made deep-learning approaches well-suited to tackle high-dimensional flow problems that feature nonlinear behaviors. Examples include transonic flow prediction over airfoils using deep learning based multi-layer perceptron neural network [41], CNN-based deep learning predictions of flow around transonic airfoils [7], transonic flow prediction by using vision transformer (ViT)-based architecture [6], using transformed-encoded geometric input, transonic flow prediction by fusing deep learning and a reduced-order model (CNN-POD) [16], to name a few. Following this, recently, graph neural networks (GNNs) [37], [24] and autoencoders [10], [44] are also developed to emulate different kinds of data-driven flow modeling. However, deep learning approaches are data hungry which can be prohibitive when expensive fluid flows are involved; furthermore, their hyperparameter tuning, despite the advances in large scale stochastic optimization, requires additional care.

We are interested in learning surrogate models capturing the parametric variation of shock-dominated fluid flows. When the underlying flowfield is smooth (that is, with continuous first derivatives with bounded Lipschitz constant), POD is known to work very well – we exploit this strength of POD in our proposed method. In short, our approach performs an invertible parametric transformation of flowfields with shocks into a smooth flowfield that is better suited to POD-based reduced basis methods; the parametric transformation is then inverted to recover the original flow field. This way, our method is generic, with just a few learnable parameters, while retaining all the advantages of POD-based ROMs; we provide more details in section 2.

1.1 Proper orthogonal decomposition (POD)

Singular value decomposition (SVD) is a commonly used matrix factorization technique that could be used to decompose the given matrix $U \in \mathbb{R}^{n \times m}$ into left orthogonal singular vectors $\Phi \in \mathbb{R}^{n \times n}$, a non-negative monotonically decreasing singular values diagonal matrix $\Sigma \in \mathbb{R}^{n \times m}$, and right orthogonal singular vectors $V \in \mathbb{R}^{m \times m}$. Consider $U = [\mathbf{u}_1, \dots, \mathbf{u}_m]$ to be our snapshot matrix, where each snapshot \mathbf{u}_i is a column vector of n elements. Mathematically, the SVD of snapshot matrix U can be written as;

$$U = \Phi \Sigma V^\top. \quad (1)$$

POD [1] is essentially applying SVD to the snapshot matrix to obtain an orthonormal basis set of vectors $\Phi = [\phi_1, \dots, \phi_n]$, also known as “POD modes”. These modes are ordered by the magnitude of the corresponding singular values $\{s_1, \dots, s_m\}$ in Σ . The singular value s_i represents the “energy” captured by the i th POD mode. According to the Eckart–Young theorem [8], the best rank- r approximation of U is given by the truncated SVD as;

$$U \approx \bar{U} = \Phi_r \Sigma_r V_r^\top, \quad (2)$$

where $\Phi_r \in \mathbb{R}^{n \times r}$ contains the first r columns of Φ (dominant modes), Σ_r is the $r \times r$ square matrix from the leading diagonal block of $\Sigma \in \mathbb{R}^{n \times m}$ and $V_r \in \mathbb{R}^{m \times r}$ contains the first r columns of V . In our problem setting, the matrix U contains a column stack of snapshot solutions for different values of parameter $\mu \in \mathcal{M} \subset \mathbb{R}^d$. Then, as described above, POD can be used to express snapshot \mathbf{u}_j via a rank- r approximation given by

$$\mathbf{u}_j \approx \sum_{i=1}^r a_i^j \phi_i, \quad (3)$$

where a_i^j is the i th component of coefficients of the basis expansion. Due to the orthonormality of the POD basis set, the coefficients \mathbf{a}^j can be expressed as

$$\mathbf{a}^j = \Phi_r^\top \mathbf{u}_j. \quad (4)$$

Crucially, every $\mathbf{a}^j = [a_1^j, \dots, a_r^j]^\top$ corresponds to a particular parameter snapshot $\mu_j \in \mathcal{M}$. If the parametric map $\mathcal{M} \rightarrow \mathbf{a}^j$, $\forall j$ is learned, e.g., via an interpolator $\hat{\mathbf{a}}$, then an unknown \mathbf{u} can be approximated as

$$\mathbf{u} \approx \hat{\mathbf{u}} = \Phi_r \hat{\mathbf{a}}. \quad (5)$$

1.2 Limitations of POD for nonsmooth data

POD-based reconstruction of flow fields offers two primary benefits: (i) linearity (which eases the inversion from $\hat{\mathbf{a}}$ to $\hat{\mathbf{u}}$) and (ii) the interpretability (in terms of capturing the high-energy coherent structures). However, these benefits can be offset when the flow field has nonsmooth features – we illustrate this with a simple example. Consider the parametric “step” function (6) which is evaluated at set of discrete points x to obtain the snapshot matrix U for different values of μ ;

$$u(x; \mu) = bH(x - \mu) \quad (6)$$

where H is the Heaviside step function, and b is a scalar that determines the height of the step (we set $b = 2$). Using this, we have generated 50 equally spaced (for $\mu \in [5, 25]$) snapshots. $x \in [0, 30]$ is discretized into 200 equally spaced points. This results in a snapshot matrix U of size 200×50 . The original data set obtained through this is shown to the left of Figure 1 below. To the right of Figure 1, we show POD reconstructions at an unseen parameter value $\mu = 14.5$, where we use a radial basis function (RBF) [11] interpolant to predict the POD coefficients at $\mu = 14.5$. Notice the “stairstepping” in the predictions, regardless of the number of modes used. Now, consider a “smoothed” version of the step function given as in which similar to (6), is evaluated at set of discrete points x to obtain the snapshot matrix U for different values of μ ;

$$u(x; \mu) = \frac{b}{1 + e^{(\mu - x)}}. \quad (7)$$

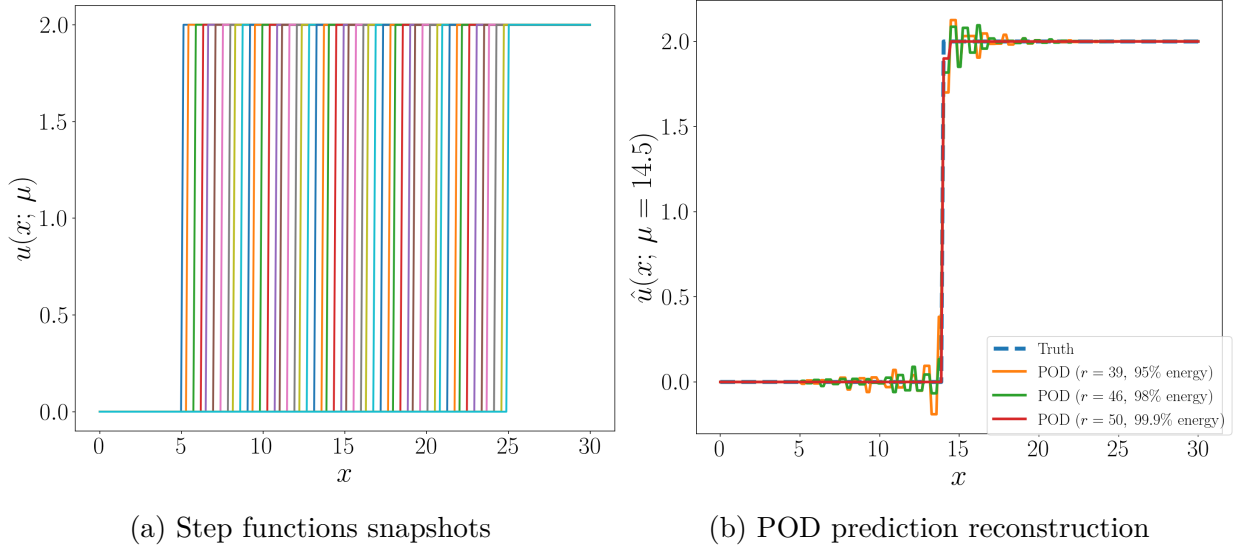


Figure 1: FOM and prediction of step function for different % energy at $\mu = 14.5$ using POD

Using this, we again generated 50 equally spaced snapshots (for $\mu \in [5, 25]$). The function snapshots and the POD reconstruction are shown in Figure 2; notice the improvement in the predictions (right) even with as few as 8 modes. This 1D example illustrates the dependence

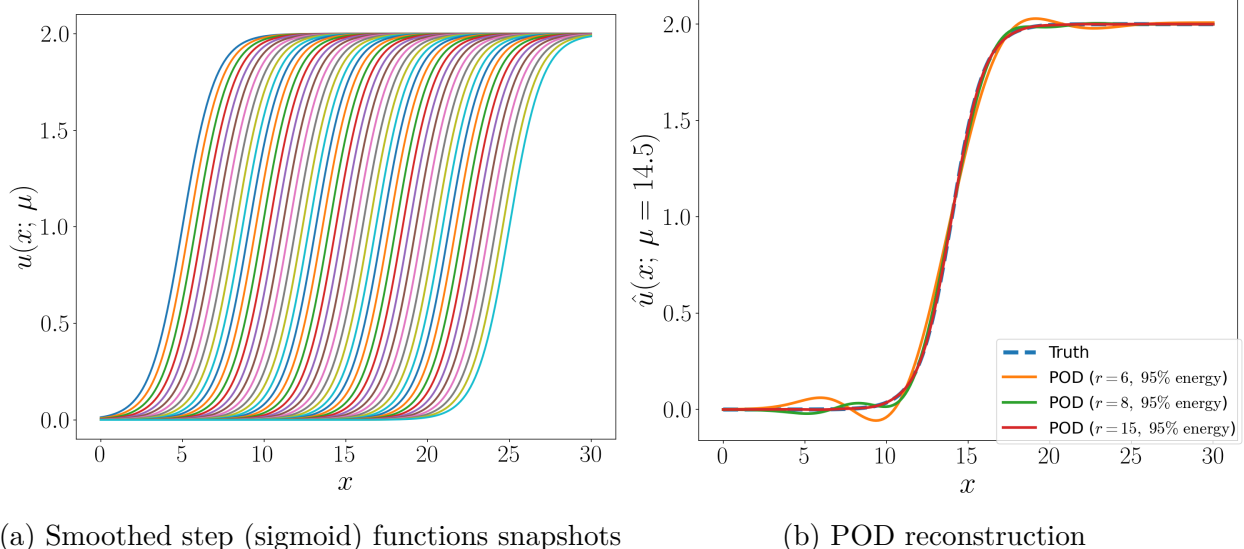


Figure 2: FOM and prediction of sigmoid function for different % energy at $\mu = 14.5$ using POD

on smoothness of the underlying snapshots for accurate POD reconstruction. The singular values plot is particularly illuminating; in Figure 3, we show the singular values for the original and smoothed snapshot matrices; notice the “slower” variation for the original snapshots (step function) compared to the smoothed snapshots. Therefore, smoothing additionally enables capturing more energy in the flow with far fewer modes than the original snapshots

– this is visualized by the bottom part of Figure 3. Drawing from this, our work proposes a strategy, where inherently nonsmooth flow fields are first smoothed using an appropriate smoothing transformation. Then, POD-based reduced basis methods are constructed on the smoothed flow fields, following which we invert the smoothing to recover the original flow fields. In this regard, we propose CRLS: convolutional regularized least squares, which uses a convolution operator to smooth flow fields for better POD reconstruction, followed by a regularized de-convolution to invert the smoothing – we provide more detail in Section 2. The rest of this paper is organized as follows. We present details of the CRLS method in

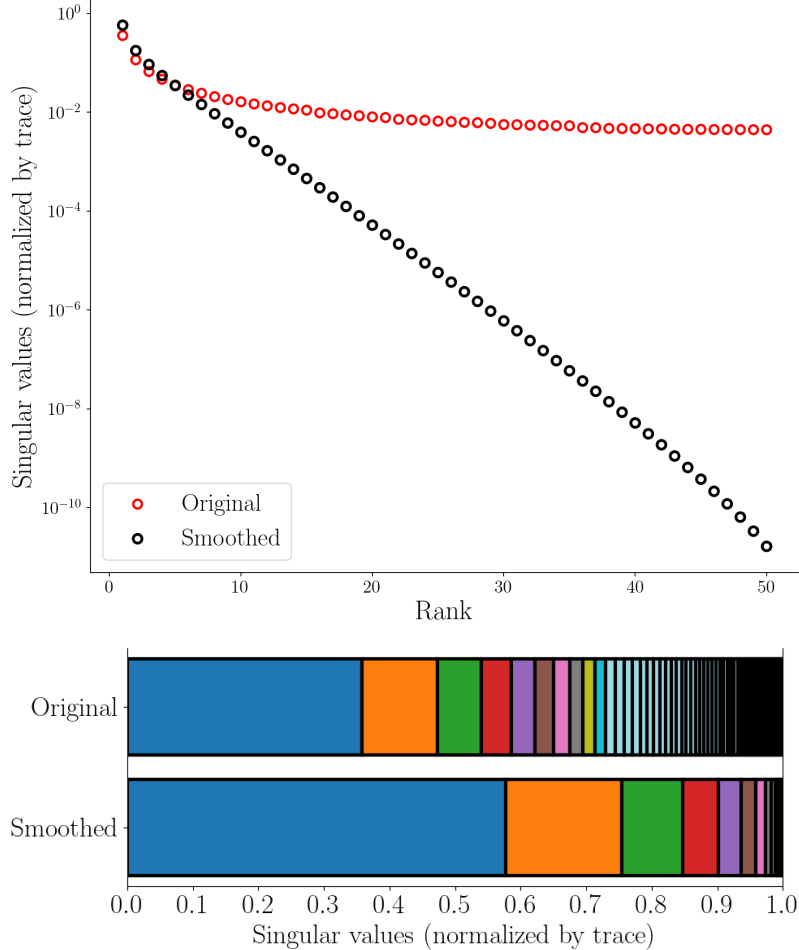


Figure 3: Comparison of normalized singular values and and cumulative contribution for step functions (original) and sigmoid functions (smoothed)

Section 2. Then, in Section 3, we present details of our experiments, followed by results and discussion in Section 3.2. Finally, we conclude in Section 4 with a summary and an outlook for future work.

2 Methodology

Our overall method **CRLS** is an amalgamation of several ingredients – we present each of them as follows.

2.1 Convolution

For two continuous functions $u(x)$ and $k(x)$, the convolution operation is defined as:

$$(u * k)(x) = \int_{-\infty}^{\infty} u(\tau) \cdot k(x - \tau) d\tau, \quad (8)$$

where τ is a dummy integration variable, which affects the width of the convolution window. In the discrete setting, eq (8) can be expressed with the integral replaced with a summation operator as

$$(u * k)(x) = \sum_{j=-\infty}^{\infty} u[j] \cdot k[x - j] \quad (9)$$

where analogous to τ in (8), j is a dummy summation index. In discrete terms, the convolution involves sliding the “filter kernel” k over the signal u . At each position, the overlapping values from the image and the kernel are multiplied element-wise and summed to produce a new value in the output smoothed/convolved snapshot. Gaussian kernel [47] is a common choice for the kernel which can be expressed as

$$k(x) = \frac{1}{\sqrt{2\pi}\sigma} \exp\left(-\frac{x}{2\sigma^2}\right), \quad (10)$$

where k is a scalar-valued function $k(x) : \mathbb{R} \rightarrow \mathbb{R}_+$, σ is the standard deviation or the measure of spread of Gaussian. In the discrete setting, the kernel is generally evaluated at odd-numbered discrete locations $x_1, x_2, x_3, \dots, x_p$, which are symmetric around zero, and normalized such that:

$$\sum_{i=1}^p k(x_i) = 1 \quad (11)$$

Consider the vector \mathbf{u}_i of n elements and let \mathbf{k} be a kernel vector of p elements obtained by evaluating (10) on a set of points $\{x_1, \dots, x_p\}$ such that $\mathbf{k} = k(\mathbf{x}) = [k(x_1), \dots, k(x_p)]^\top$; note that $p < n$ necessarily. In the context of 1D Gaussian smoothing, convolution is used to apply the Gaussian kernel to the snapshot data matrix sequentially (one snapshot at a time) to produce a smoothed version of the data matrix U . For simplicity, the convolved value in the discrete case, i.e., for a sampled snapshot \mathbf{u}_i at index j can be expressed as:

$$\mathbf{u}_i^s[j] = \sum_{l=1}^p \mathbf{u}_i[(j - 1 + l)] \cdot k(x_l), \quad (12)$$

where $\mathbf{u}_i^s[j]$ is the convolved value of \mathbf{u}_i at index j . This means that each new smoothed value of \mathbf{u}_i is computed as a weighted sum of a set of p elements of $\mathbf{u}_i[j]$, where the weights are determined by the Gaussian kernel k .

This smoothing process, which involves a moving window of p elements, needs special attention to ensure the smoothed snapshot retains the cardinality of the original nonsmooth

snapshot. This is illustrated as follows: consider the snapshot \mathbf{u}_i of six elements and kernel window of three elements, then the convolved output snapshot \mathbf{u}_i^s would have four elements as shown in the Figure 4. To overcome this problem, padding is generally used to extend

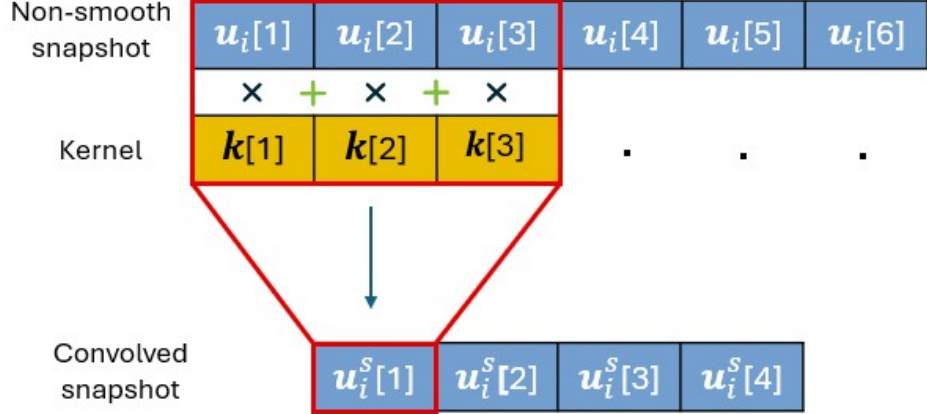


Figure 4: Convolution without padding

the length of \mathbf{u}_i before applying the convolution. For a kernel window \mathbf{k} of p elements, L additional elements are added for the padding. Multiple types of padding such as zero padding, constant padding, and reflect padding can be used. The choice of padding affects how smoothly the edges are handled. To prevent abrupt changes in the convolved values without compromising the quality of data, we have used the reflect padding here. Consider again the same snapshot \mathbf{u}_i of six elements and kernel window of three elements. The snapshot now has 1 additional element on each side as a padding (reflect padding). The convolved output snapshot \mathbf{u}_i^s , thus, would now have six elements as shown in Figure 5.

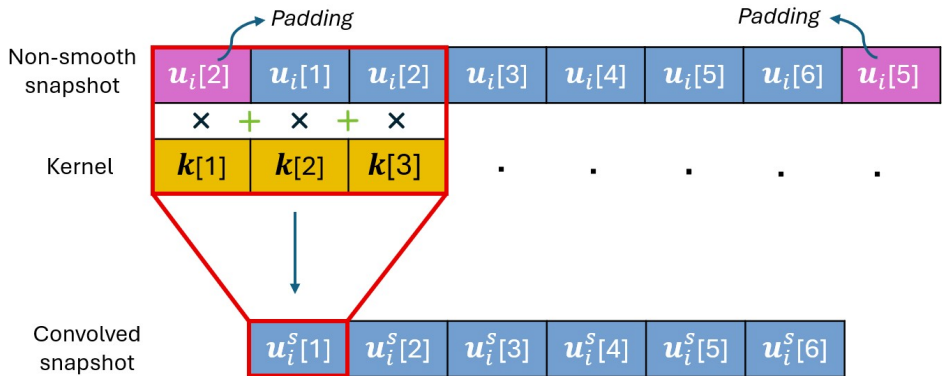


Figure 5: Convolution with reflect padding

2.2 Reflect-padded 1D convolution in matrix form

In this subsection, we will provide the details of mathematical formulation to perform the convolution with the reflect-padded data using the kernel in the matrix form. Consider again the input snapshot data \mathbf{u}_i of n elements and kernel \mathbf{k} of p elements, then to have the

smoothened output \mathbf{u}_i^s of same cardinality as input \mathbf{u}_i , a padding size L is chosen as:

$$L = \frac{(p-1)}{2}, \quad (13)$$

where p is the kernel length, and notice that p must be an odd number for L to be an integer. This padding will extend \mathbf{u}_i with n elements to another vector $\tilde{\mathbf{u}}_i$ with $n+2L$ total elements. Consider a set of indices $\{j \in \mathbb{Z} \mid -L \leq j \leq n+L-1\}$, then $\tilde{\mathbf{u}}_i$ can be written as

$$\tilde{\mathbf{u}}_i = \begin{cases} \mathbf{u}_i[-j], & \text{if } -L \leq j < 0, \\ \mathbf{u}_i[j], & \text{if } 0 \leq j \leq n, \\ \mathbf{u}_i[2n-2-j], & \text{if } n < j \leq n+L. \end{cases} \quad (14)$$

Note that we introduce negative indices $\{-L, -L+1, \dots, 0\}$ to preserve the fact that indices $\{1, \dots, n\}$ corresponds to the original snapshot. This way, the front padding $(-L, \dots, 0)$ mirrors the first L elements of the snapshot, the rear padding $(n+1, \dots, n+L)$ mirrors the last L elements of the snapshot and the rest are unchanged. The reason for doing this will become clear next: the convolved snapshot \mathbf{u}_i^s can be written as

$$\mathbf{u}_i^s[j] = \sum_{l=1}^p \tilde{\mathbf{u}}_i[(j-1+l)] \cdot \mathbf{k}[l], \quad \forall j = 1, \dots, n. \quad (15)$$

It is also possible to write the convolved output \mathbf{u}_i^s , $\forall i$ in matrix form as $\mathbf{U}^s = \mathbf{B}\mathbf{U}$ if we define \mathbf{B} to be an $n \times n$ matrix with entries $B_{i,j}$ given by:

$$B_{i,j} = \begin{cases} k_q, & \text{if } (i+q-L < 0 \text{ and } j = -(i+q-L)) \\ & \text{or } (0 \leq i+q-L < n \text{ and } j = i+q-L) \\ & \text{or } (i+q-L \geq n \text{ and } j = 2n-2-(i+q-L)), \\ 0, & \text{otherwise.} \end{cases} \quad (16)$$

where $q \in \{0, \dots, p-1\}$. We illustrate the construction of the \mathbf{B} matrix for a simple case of $p=3$ and $L=5$ in Appendix A.

2.3 Deconvolution

The process of inverting a convolution is called deconvolution, which is a lossy operation and is generally difficult to recover the original data from it exactly. With the information about how the convolution is performed, as presented above i.e; $\mathbf{u}_i^s = \mathbf{B}\mathbf{u}_i$, one can perform the deconvolution to invert \mathbf{u}_i from \mathbf{u} by minimizing the residual $\frac{1}{2}\|\mathbf{B}\mathbf{u}_i - \mathbf{u}_i^s\|^2$. However, to overcome the ill-conditioning of \mathbf{B} (which leads to the lossiness of this inversion), we regularize the residual $\frac{1}{2}\|\mathbf{B}\mathbf{u}_i - \mathbf{u}_i^s\|^2$ accordingly – this leads to our convolutional regularized least squares (CRLS) method. We will provide more detail on this regularization momentarily, but before that, we will address how to estimate the hyperparameters of the convolution operation next.

2.4 Estimation of hyperparameters

The extent of smoothing in our convolution operation is affected by the Gaussian width σ and the size of the kernel window $\text{len}(\mathbf{k})$. $\text{len}(\mathbf{k})$ is an integer varying from 1 to n and $\sigma \in [0, \infty)$ is a nonnegative real-valued parameter. At $\sigma = 0$ the Gaussian becomes a Dirac delta function, i.e., no smoothing at all; on the other hand, as $\sigma \rightarrow \infty$, the Gaussian flattens out and becomes constant, and the snapshots will be completely blurred, i.e., no variation at all. In practice, the range of σ for Gaussian smoothing is meaningful only within certain bounds. On the other hand, having a smaller kernel window, which, while resulting in a sparse matrix B , eases the deconvolution computation, can lead to insufficient smoothing. And, vice versa, larger kernel windows are also undesirable.

We formulate an optimization problem to optimally estimate these two hyperparameters. Specifically, we choose hyperparameters by minimizing the maximum infinity norm of the prediction error over a “held out” test set of snapshots. This is presented as follows

$$\begin{aligned} \{\sigma^*, \text{len}(\mathbf{k})^*\} = & \arg \min_{\sigma, \text{len}(\mathbf{k})} \max_{i \in \mathcal{T}} \|\mathbf{u}_{i,\text{predict}} - \mathbf{u}_i\|_\infty \\ \text{s.t. } & \sigma \in [0, 100] \subset \mathbb{R} \\ & \text{len}(\mathbf{k}) \in [1, \text{len}(\mathbf{u})] \subset \mathbb{N}, \end{aligned} \quad (17)$$

where \mathcal{T} is a set of indices corresponding to the held out snapshot set, $\mathbf{u}_{i,\text{predict}}$ is the predicted snapshot after deconvolution at an unseen parameter location, and \mathbf{u}_i is an original snapshot in the held out set. The bounds on $\text{len}(\mathbf{k})$ are natural, and the bounds on σ are chosen based on experiments with a variety of ranges; note that one can still set $0 \leq \sigma < \infty$, and our method works seamlessly, but we recommend a finite range. Solving this minimax problem is hard without access to gradients and due to the fact that the max operator being non-differentiable. Therefore, we solve it using Bayesian optimization [12, 26, 31, 32, 30] with Gaussian process [25] surrogate models.

2.5 Least squares regularization

Once we have the hyperparameters estimated for the convolution, we are ready to pose and solve our regularized least squares optimization problem to invert the smoothed prediction \mathbf{u}^s to obtain the prediction with shocks \mathbf{u} . In this work, we regularize the least squares problem with the Euclidean distance to a reference snapshot \mathbf{u}_{ref} . The CRLS optimization problem is then given as

$$\mathbf{u}_{\text{predict}} = \min_{\mathbf{u}} \frac{1}{2} \|B\mathbf{u} - \mathbf{u}^s\|_2^2 + \frac{\gamma}{d^2} \|\mathbf{u} - \mathbf{u}_{\text{ref}}\|_2^2, \quad (18)$$

where \mathbf{u} is the unknown solution to be determined, \mathbf{u}^s is the predicted smooth snapshot after convolution, γ is the regularization parameter, d is a weighting parameter, and \mathbf{u}_{ref} is the reference snapshot chosen to be the nearest neighbor (in the parameter space) to the current parameter of interest μ ; we use a KDTree (implemented as `KDTree` in SciPy [43]) based nearest neighbor algorithm for this purpose. The weighting parameter measures the Euclidean distance, in the parameter space, between μ and μ_{ref} . This inverse squared-distance weighting follows the intuition that for parameters close by in parameter space, the corresponding

snapshots are likely to be close by in the snapshot space. Finally, the POD coefficients at unseen parameter locations are interpolated via a radial basis function (RBF) interpolant, for which we use the Rbf implementation in SciPy.

The complete algorithm consists of two distinct parts. The offline part, which needs to run once for a unique set of snapshot data, will perform convolution and POD basis extraction, following the hyperparameter estimation. Next, the online part includes prediction and regularized least squares inversion. The overall methodology is summarized in Figure 6.

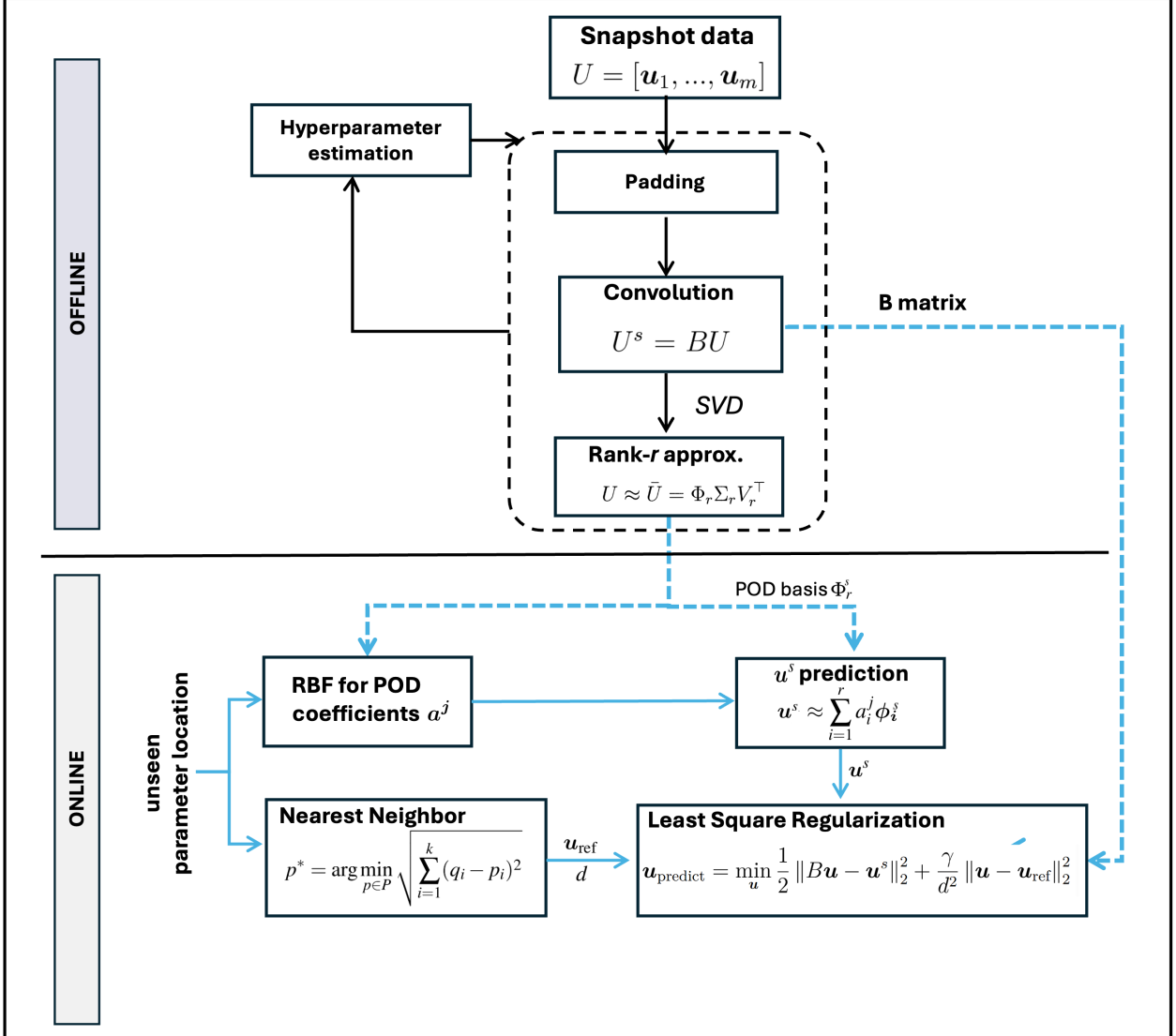


Figure 6: CRLS algorithm overview

3 Experiments

We demonstrate our methodology on the transonic flow past the RAE2822 airfoil. For the full order model (FOM), we consider the two-dimensional, steady, compressible Euler equations

to model fluid flow. These equations capture the conservation of mass, momentum, and energy and are summarized as follows:

$$\begin{aligned} (\rho u)_x + (\rho v)_y &= 0, \\ (\rho u^2 + p)_x + (\rho u v)_y &= 0, \\ (\rho u v)_x + (\rho v^2 + p)_y &= 0, \\ (\rho u H)_x + (\rho v H)_y &= 0. \end{aligned} \tag{19}$$

where

$$H = E + \frac{p}{\rho}, \quad E = \frac{u^2 + v^2}{2} + \frac{p}{\rho(\gamma - 1)}.$$

Here, u and v are x and y-components of the velocity, ρ is the density, p is pressure, E is internal energy, H is the enthalpy, and γ is the adiabatic index. We use the open-source finite-volume-based CFD solver SU2 [9] to solve the FOM and generate the snapshot data. Assuming a quasi-1D, irrotational flow in the boundary-normal direction, the free-stream values at boundary faces are then computed by extrapolating Riemann invariants. The numerical solution uses a second-order spatial discretization and a coupled implicit method with a hybrid Gauss-least-squares method for gradient computations. Lastly, to handle steep gradients (shocks), the Venkatakrishnan limiter is used for the numerical stability of the solution. On the airfoil surface, an adiabatic slip-wall condition is imposed, and by using reconstruction gradients, primitive and thermodynamic variables are extrapolated from the interior of the domain. This provides a robust and accurate framework for capturing shocks in transonic flow over the airfoil to generate FOM snapshots.

The RAE2822 airfoil is a widely used canonical transonic aerodynamics test case. To model the farfield domain, we use a circular region with a radius set to 100 times the chord length of the airfoil, with an O-grid structured mesh of 32,900 cells and near-field mesh refinement for accurate capture of the shock wave. We collect snapshots of the pressure coefficient (C_p) defined as:

$$C_p = \frac{p - p_\infty}{\frac{1}{2} \rho_\infty (M_\infty a_\infty)^2} \tag{20}$$

where p is the local pressure, p_∞ and ρ_∞ are the free-stream pressure and density, and M_∞ and a_∞ are the free-stream Mach number and speed of sound, respectively.

3.1 Training and test data generation

We consider two control parameters: the Mach number $M \in [0.8, 0.9]$, and the angle of attack: for which we set the range and the angle of attack $\alpha \in [0, 2]$. The parameter ranges are selected to ensure that the flow almost always includes a shock somewhere along the airfoil while also demonstrating substantial changes in the shock location. We generate a design of experiment, via Latin hypercube sampling [20], with 90 experiments total. Of this 90, we hold out 5 for final validation; we split the remaining 85 as a 90% - 10% partition for hyperparameter learning in the offline phase. The parameter scatterplot, with training and validation points highlighted, is shown in Figure 7.

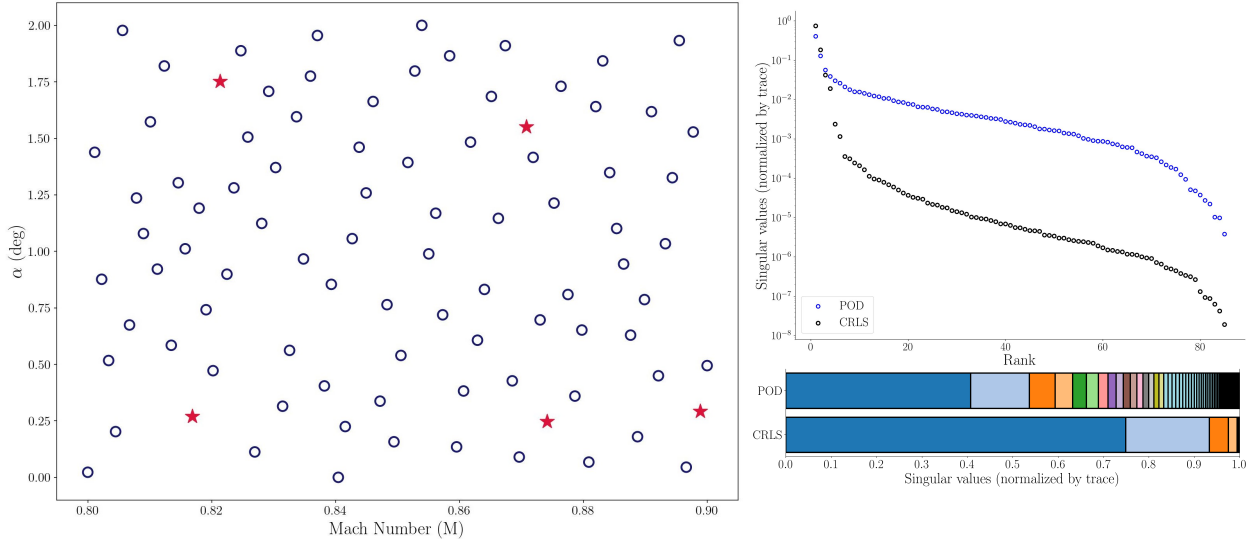


Figure 7: Design of experiments and verification data points

3.2 Results and discussion

We entertain three different reduced basis approaches: a traditional approach of applying POD to the snapshots without any smoothing (POD), POD applied to the smoothed snapshots but without regularization (POD-c), and the proposed approach (CRLS). The singular values plot shown in Figure 7 echoes the same trend observed with the 1-D step and sigmoid function (Figure 2) – that is, smoothing restructures the energy distribution amongst the modes, allowing more energy to be captured by fewer modes. Specifically, after smoothing, we notice that the first singular value corresponds to roughly 75% of the energy, and the second singular value corresponds to about 18% of the energy – so 93% of the total energy is captured by the first two modes. Overall, 99.99% of the total energy is captured by 48 modes in the case of smoothed snapshots, in contrast to 81 modes in the case of the original (nonsmooth) snapshots.

3.2.1 Airfoil surface pressure coefficients prediction

Figure 8 shows the predicted pressure coefficients (C_p) obtained from each of the three reduced basis approaches and the true C_p obtained from solving the FOM. We retain modes that account for roughly 99.9% of the total energy. From these plots, it is quite evident that conventional approaches (without smoothing) lead to stair-stepping in the reconstructed solution, which is unsurprising. However, without regularization, even the PODc approach can lead to stair-stepped predictions, as illustrated in these figures; this is attributed to the ill-conditioning of the smoothing matrix B . On the other hand, the proposed CRLS method predicts physically consistent distributions that are very close to the FOM solution. Overall, the CRLS predictions are uniformly accurate across all the 5 validation parameters.

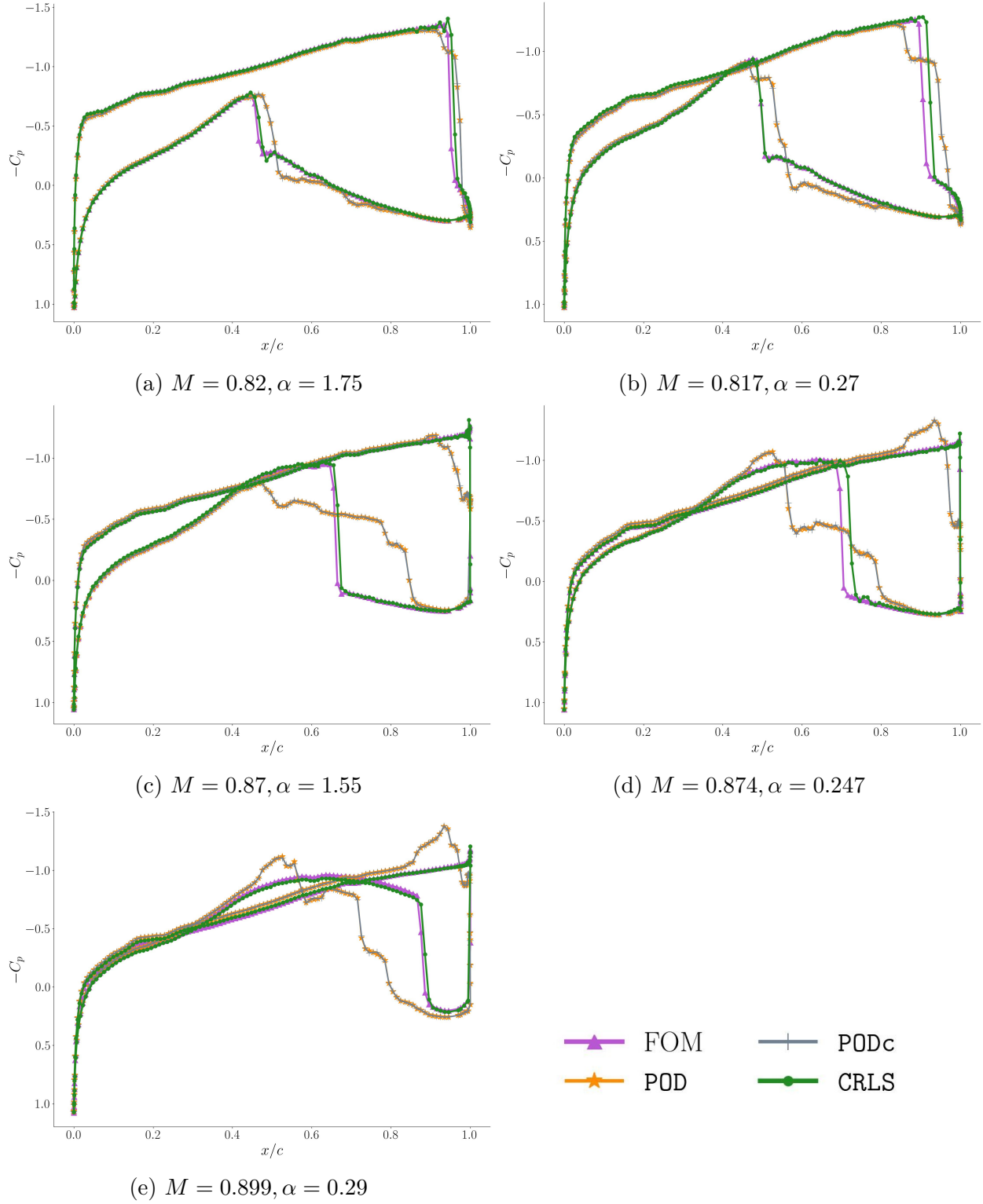


Figure 8: Comparison of pressure coefficient (C_p) distribution on the airfoil surface.

3.2.2 Full pressure field predictions

Section 3.2.2 shows the predictions of the full pressure coefficient field in the flow domain for the same set of parameters in Figure 8; note that we only show a close-up view of the airfoil in the figures. Here we include only the PODc in the comparison. Notice that PODc results in the non-physical “double shocks” on the upper and lower surfaces, which is consistent with the stair-stepping observed in the C_p plots. On the other hand, the CRLS predicts physically consistent fields that are quite similar to the FOM solutions. We provide a visualization of the pointwise error fields next.

To quantify the prediction error, we begin by observing the mean absolute errors (MAE) and root mean squared error (RMSE) shown in figures 11 and 12, respectively. For a set of N spatial locations with prediction \mathbf{u} and FOM reference \mathbf{u}^{FOM} , these are written as

$$\text{MAE} = \frac{1}{N} \|\mathbf{u} - \mathbf{u}^{\text{FOM}}\|_1, \quad \text{RMSE} = \sqrt{\frac{1}{N} \|\mathbf{u} - \mathbf{u}^{\text{FOM}}\|_2^2}. \quad (21)$$

Whereas MAE measures the average pointwise deviation, RMSE penalizes larger local errors more. Notice that both POD and PODc give almost the same error, with PODc being slightly lower. Unsurprisingly, the CRLS gives the lowest MAE and RMSE while surpassing the other two approaches by a substantial margin.

We then compute the absolute difference between the predicted and true fields and visualize their contours, shown in Figure 10. Similar to airfoil surface pressure results, POD and PODc show similar error contours. Notably, PODc requires only about 48 modes, while POD requires 81 modes out of 85, to capture the same amount of energy. From the error contours, it can also be observed that the shock locations for POD and PODc are significantly different from those for CRLS despite requiring far fewer modes.

Implementation details. To keep the convolution and deconvolution operations in CRLS tractable, we must take some measures. Specifically, the arrangement of the snapshots on a structured grid can drastically improve the computational complexity of these operations. To enable this, we interpolate snapshots on unstructured grids onto a structured “O-grid” – we show an illustration in Figure 13.

4 Conclusions

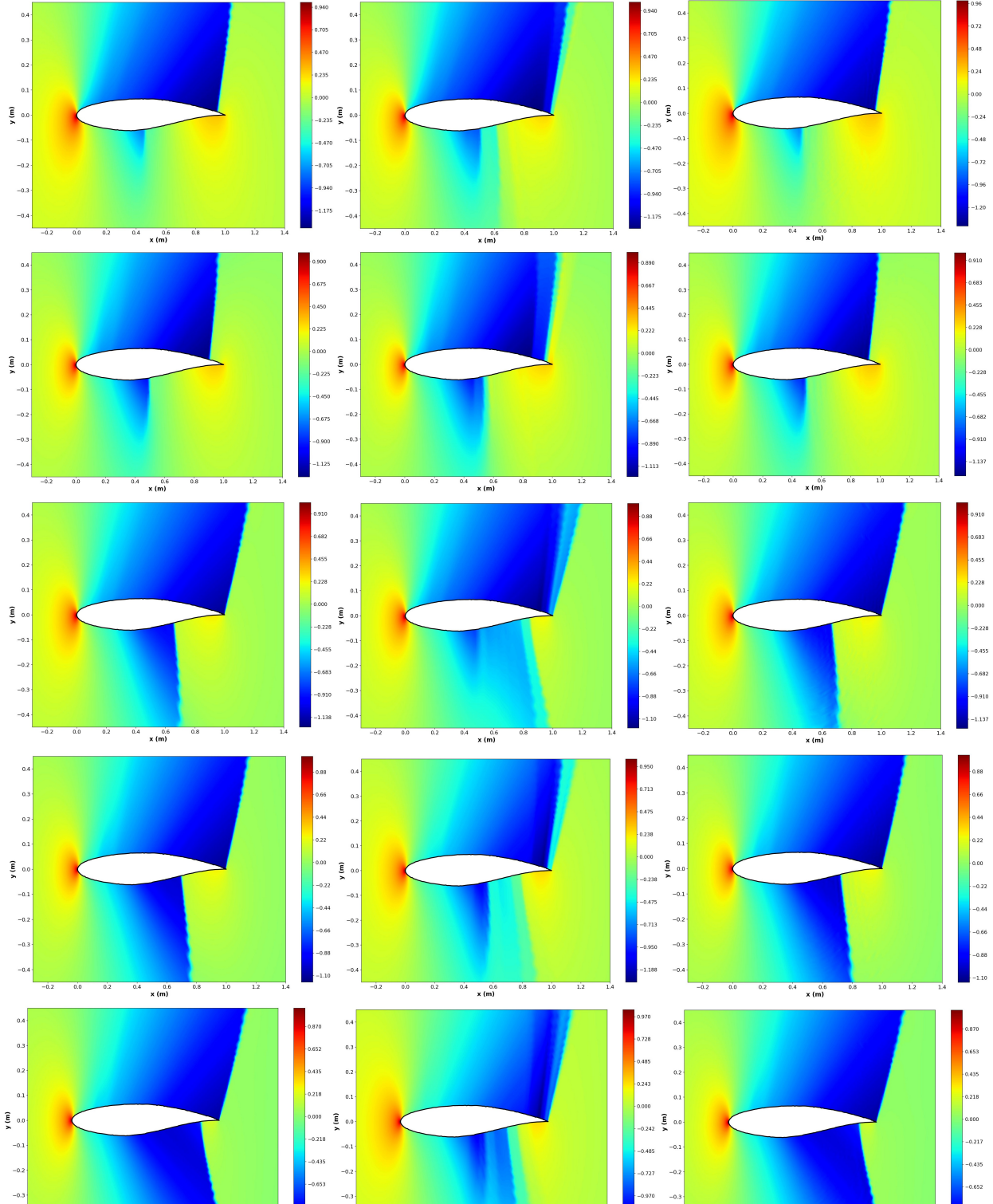
In this work we have introduced a CRLS (convolutional regularized least squares) framework for building reduced-order models of flows with parameter-dependent shocks. The central idea is to exploit the fact that proper orthogonal decomposition (POD) is most effective when applied to smooth fields; we first map snapshots containing sharp gradients into a smoother space via a one-dimensional Gaussian convolution with reflect padding, construct POD bases and interpolate POD coefficients in that space, and then reconstruct sharp features by solving a regularized deconvolution problem. The convolution hyperparameters and the deconvolution regularization are selected automatically by solving targeted optimization problems, so that the entire procedure is largely data-driven and requires minimal user tuning.

A simple one-dimensional step function example illustrates the main mechanism: smoothing dramatically accelerates the decay of the singular values and allows POD to capture the dominant behavior with far fewer modes, while the deconvolution step recovers sharp transitions that are otherwise smeared or stair-stepped. We then applied CRLS to a more realistic and challenging setting – steady, inviscid, transonic flow over the RAE2822 airfoil governed by the compressible Euler equations. For this configuration, CRLS consistently produced pressure coefficient distributions and full pressure fields that closely track the full-order model, while standard POD and a purely smoothed POD (without regularized inversion) exhibited non-physical oscillations, double shocks, and noticeable shock misplacement. Quantitatively, the proposed method yields the lowest mean absolute error and root-mean-square error across all validation cases and achieves a significant reduction in the number of POD modes required to represent a fixed fraction of snapshot energy, translating directly into lower online evaluation costs.

Beyond these specific results, CRLS has several practical advantages. It operates non-intrusively on snapshot data and therefore can be wrapped around existing CFD solvers without modifying their discretizations or numerics. The reflect-padded convolution and its matrix representation are compatible with structured grids obtained from interpolating unstructured meshes (such as O-grids), which keeps both the smoothing and inversion steps computationally tractable. The use of Bayesian optimization to tune the convolution kernel width and support, coupled with nearest-neighbor regularization in parameter space, makes the approach adaptable to different flow regimes and parameter ranges with minimal manual intervention.

Despite its promising performance, the present CRLS framework has a few limitations. First, the method relies on mapping snapshots to a structured O-grid and applying a one-dimensional Gaussian convolution with fixed orientation; while this is done to make the computational complexity of the approach tractable, more innovative methods to perform the convolution and deconvolution can further enhance the method. Second, CRLS uses radial basis function interpolation and a nearest-neighbor reference in parameter space; both ingredients assume reasonably dense sampling and are not designed for aggressive extrapolation beyond the training envelope. Finally, the current implementation does not explicitly enforce physical constraints such as conservation or stability of long-time integrations, and the impact of noisy or inconsistent snapshot data on the regularized inversion has not been systematically quantified; addressing these issues will be important for deploying CRLS in broader aerodynamic design and control workflows.

The present study focuses on steady, inviscid, two-dimensional transonic aerodynamics; however, the methodology is more general. Future work will extend CRLS to viscous and turbulent flows, unsteady problems, and three-dimensional configurations of interest. It will also be valuable to explore alternative kernels and anisotropic or directionally aligned convolutions, richer regularization strategies that encode physical constraints, and combinations of CRLS with hyper-reduction or data-driven closure models. Finally, embedding CRLS-based surrogates into optimization and uncertainty quantification loops, for example in reliability-based design or multiobjective aerodynamic optimization, offers a promising avenue to obtain shock-resolving reduced-order models that remain both accurate and computationally affordable at scale.



(a) FOM

(b) (Naive) POD

(c) CRLS (ours)

Figure 9: Comparison of pressure coefficient (C_p) contours. Each row corresponds to parameter values in panels (a) through (e) in Figure 8.

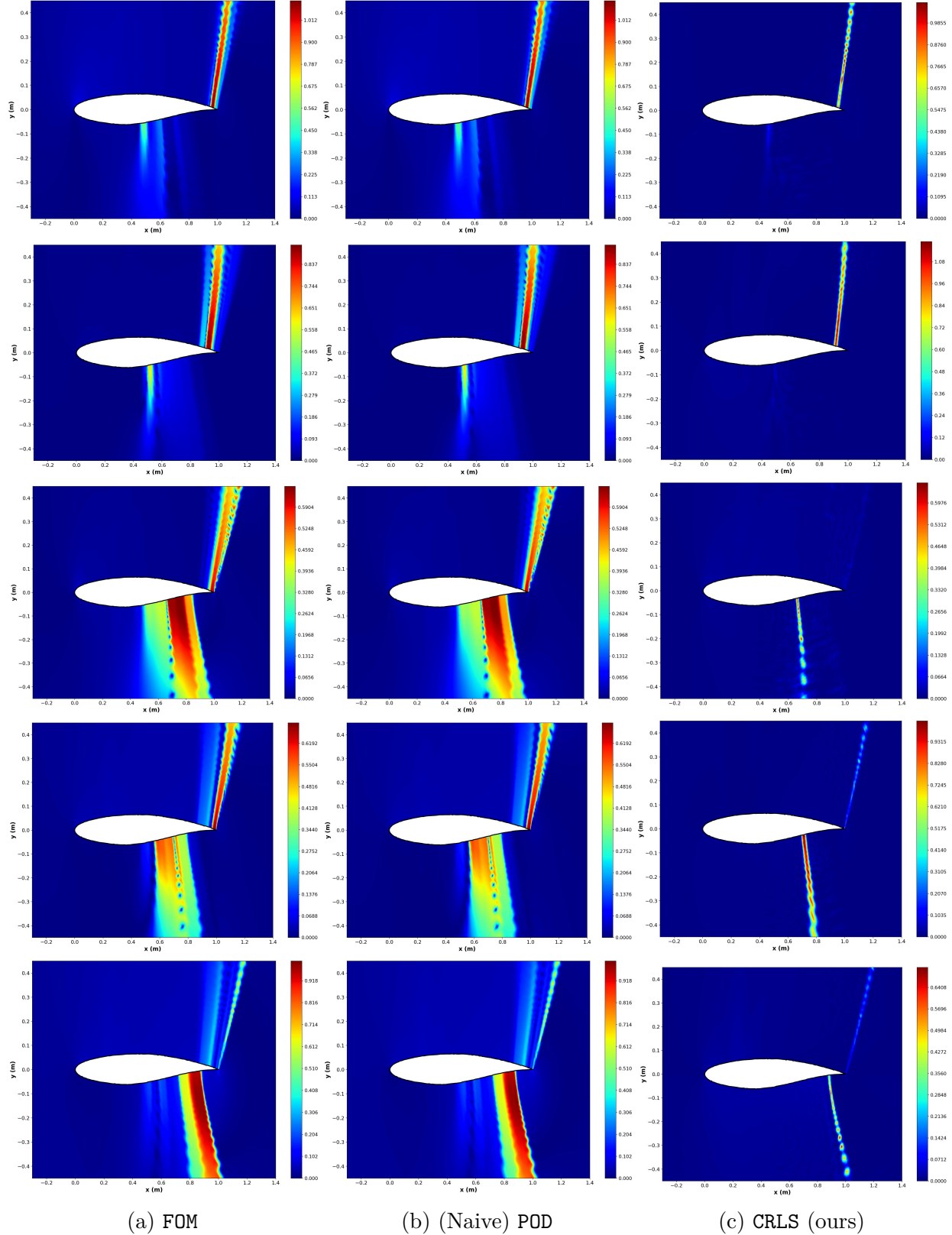


Figure 10: Comparison of the mean absolute error in pressure coefficient (C_p) contours. Each row corresponds to parameter values in panels (a) through (e) in Figure 8.

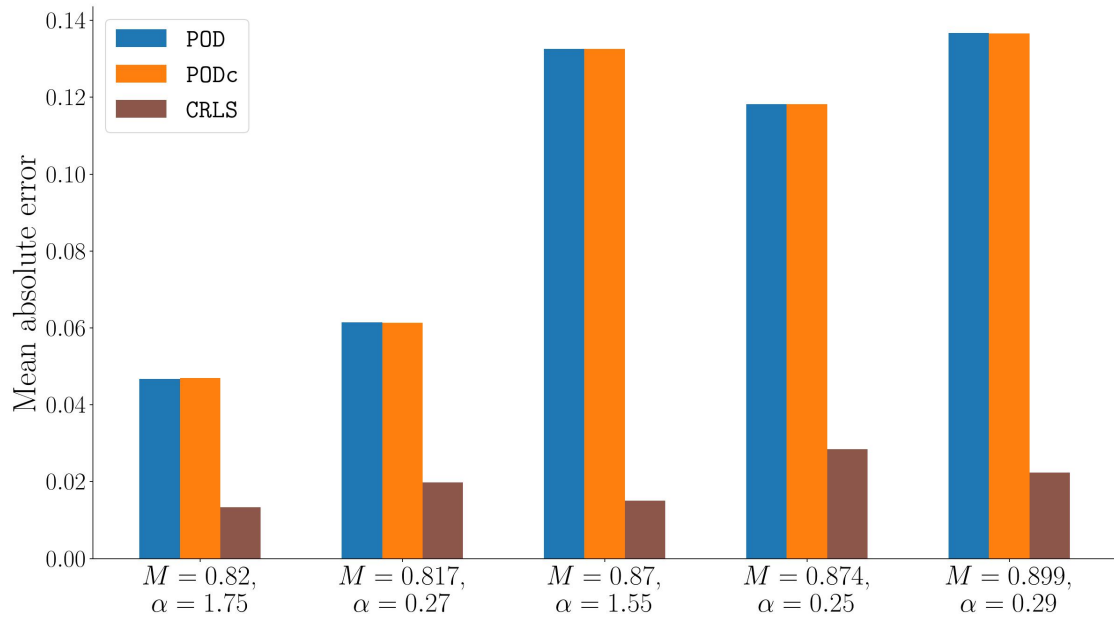


Figure 11: Mean absolute error of C_p on airfoil surface

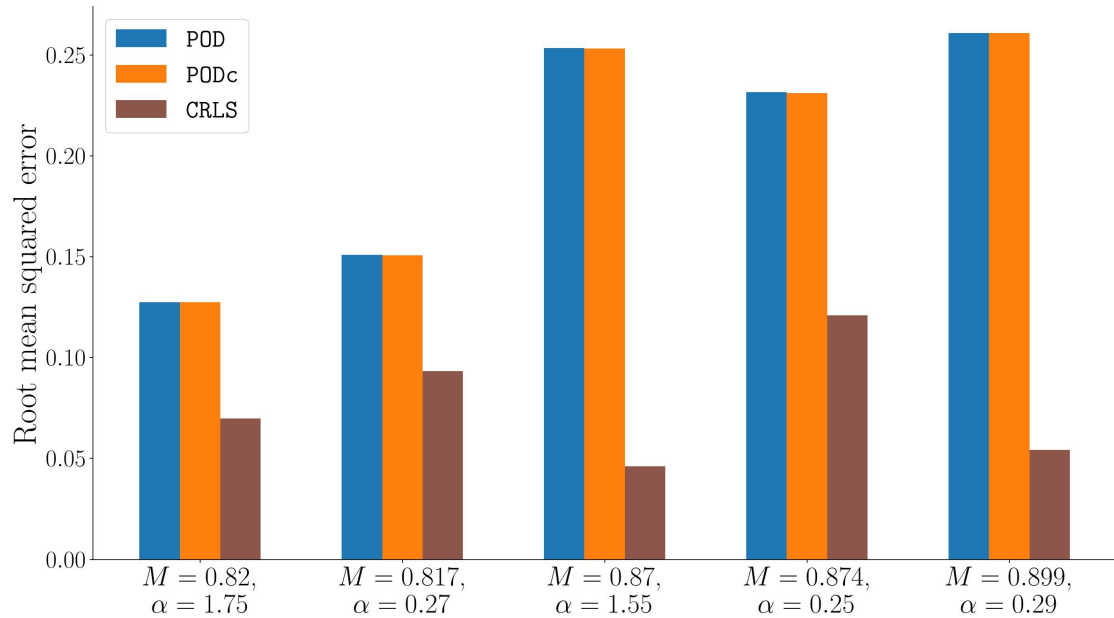


Figure 12: Root mean squared error of C_p on airfoil surface

References

- [1] Gal Berkooz, Philip Holmes, and John L. Lumley. The proper orthogonal decomposition in the analysis of turbulent flows. *Annual Review of Fluid Mechanics*, 25:539–575, 1 1993. ISSN 00664189. doi: 10.1146/annurev.fl.25.010193.002543.
- [2] Saakaar Bhatnagar, Yaser Afshar, Shaowu Pan, Karthik Duraisamy, and Shailendra Kaushik. Prediction of aerodynamic flow fields using convolutional neural networks. *Computational Mechanics*, 64:525–545, 8 2019. ISSN 01787675. doi: 10.1007/s00466-019-01740-0.
- [3] Kevin Carlberg. Adaptive h-refinement for reduced-order models. *International Journal for Numerical Methods in Engineering*, 102:1192–1210, 5 2014. ISSN 1097-0207. doi: 10.1002/nme.4800.
- [4] Bernardo Cockburn and Chi Wang Shu. The runge–kutta discontinuous galerkin method for conservation laws v: Multidimensional systems. *Journal of Computational Physics*, 141:199–224, 4 1998. ISSN 0021-9991. doi: 10.1006/jcph.1998.5892.
- [5] Yuanjun Dai, Yiran An, Zhi Li, Jihua Zhang, and Chao Yu. Fourier neural operator with boundary conditions for efficient prediction of steady airfoil flows. *Applied Mathematics and Mechanics (English Edition)*, 44:2019–2038, 11 2023. ISSN 15732754. doi: 10.1007/s10483-023-3000-7.
- [6] Zhiwen Deng, Jing Wang, Hongsheng Liu, Hairun Xie, Bo Kai Li, Miao Zhang, Tingmeng Jia, Yi Zhang, Zidong Wang, and Bin Dong. Prediction of transonic flow over supercritical airfoils using geometric-encoding and deep-learning strategies. *Physics of Fluids*, 35, 7 2023. ISSN 10897666. doi: 10.1063/5.0155383.
- [7] Cihat Duru, Hande Alemdar, and Ozgur Ugras Baran. A deep learning approach for the transonic flow field predictions around airfoils. *Computers and Fluids*, 236, 1 2022. ISSN 00457930. doi: 10.1016/j.compfluid.2022.105312.
- [8] Carl Eckart and Gale Young. The approximation of one matrix by another of lower rank. *Psychometrika*, 1(3):211–218, 1936. doi: 10.1007/BF02288367.
- [9] Thomas D Economon, Francisco Palacios, Sean R Copeland, Trent W Lukaczyk, and Juan J Alonso. Su2: An open-source suite for multiphysics simulation and design. *Aiaa Journal*, 54(3):828–846, 2016. doi: 10.2514/1.J053813.
- [10] Hamidreza Eivazi, Hadi Veisi, Mohammad Hossein Naderi, and Vahid Esfahanian. Deep neural networks for nonlinear model order reduction of unsteady flows. *Physics of Fluids*, 32, 10 2020. ISSN 10897666. doi: 10.1063/5.0020573.
- [11] Gregory E. Fasshauer. *Meshfree Approximation Methods with MATLAB*. World Scientific Publishing Company, Singapore, 2007. ISBN 978-981-270-633-1.
- [12] Peter I. Frazier. *Bayesian Optimization*, chapter 11, pages 255–278. doi: 10.1287/educ.2018.0188.

- [13] Lin Fu, Xiangyu Y. Hu, and Nikolaus A. Adams. A family of high-order targeted eno schemes for compressible-fluid simulations. *Journal of Computational Physics*, 305: 333–359, 1 2016. ISSN 10902716. doi: 10.1016/j.jcp.2015.10.023.
- [14] R. Fu, D. Xiao, I. M. Navon, F. Fang, L. Yang, C. Wang, and S. Cheng. A non-linear non-intrusive reduced order model of fluid flow by auto-encoder and self-attention deep learning methods. *International Journal for Numerical Methods in Engineering*, 124: 3087–3111, 7 2023. ISSN 10970207. doi: 10.1002/nme.7174.
- [15] Abdul J. Jerri. *The Gibbs Phenomenon in Fourier Analysis, Splines and Wavelet Approximations*. Springer, 1998. doi: 10.1007/978-1-4757-2847-7.
- [16] Xuyi Jia, Chunlin Gong, Wen Ji, and Chunna Li. An accuracy-enhanced transonic flow prediction method fusing deep learning and a reduced-order model. *Physics of Fluids*, 36, 5 2024. ISSN 10897666. doi: 10.1063/5.0204152.
- [17] Guang-Shan Jiang and Chi-Wang Shu. Efficient implementation of weighted eno schemes. *Journal of Computational Physics*, 126:202–228, 6 1996. ISSN 0021-9991. doi: 10.1006/jcph.1996.0130.
- [18] J. Nathan Kutz. Deep learning in fluid dynamics. *Journal of Fluid Mechanics*, 814:1–4, 3 2017. ISSN 0022-1120. doi: 10.1017/jfm.2016.803.
- [19] Zongyi Li, Nikola B. Kovachki, Kamyar Azizzadenesheli, Burigede Liu, Kaushik Bhattacharya, Andrew M. Stuart, and Anima Anandkumar. Fourier neural operator for parametric partial differential equations. In *Proceedings of the 9th International Conference on Learning Representations (ICLR)*, 2021. doi: 10.48550/arXiv.2010.08895.
- [20] Wei-Liem Loh. On latin hypercube sampling. *The annals of statistics*, 24(5):2058–2080, 1996. doi: 10.1214/aos/1069362310.
- [21] Romit Maulik, Bethany Lusch, and Prasanna Balaprakash. Reduced-order modeling of advection-dominated systems with recurrent neural networks and convolutional autoencoders. *Physics of Fluids*, 33, 3 2021. ISSN 10897666. doi: 10.1063/5.0036985.
- [22] Nirmal J. Nair and Maciej Balajewicz. Transported snapshot model order reduction approach for parametric, steady-state fluid flows containing parameter-dependent shocks. *International Journal for Numerical Methods in Engineering*, 117:1234–1262, 3 2019. ISSN 10970207. doi: 10.1002/nme.5998.
- [23] Samuel E. Otto, Gregory R. Macchio, and Clarence W. Rowley. Learning nonlinear projections for reduced-order modeling of dynamical systems using constrained autoencoders. *Chaos*, 33, 11 2023. ISSN 10897682. doi: 10.1063/5.0166302.
- [24] Jiang Zhou Peng, Yue Hua, Yu Bai Li, Zhi Hua Chen, Wei Tao Wu, and Nadine Aubry. Physics-informed graph convolutional neural network for modeling fluid flow and heat convection. *Physics of Fluids*, 35, 8 2023. ISSN 10897666. doi: 10.1063/5.0161114.

[25] Carl Edward Rasmussen and Christopher K. I. Williams. *Gaussian Processes for Machine Learning*. The MIT Press, 11 2005. ISBN 9780262256834. doi: 10.7551/mitpress/3206.001.0001.

[26] Ashwin Renganathan and Kade Carlson. *qPOTS*: Efficient batch multiobjective Bayesian optimization via pareto optimal Thompson sampling. In *International Conference on Artificial Intelligence and Statistics*, pages 4051–4059. PMLR, 2025.

[27] S. Ashwin Renganathan. Koopman-based approach to nonintrusive reduced order modeling: Application to aerodynamic shape optimization and uncertainty propagation. *AIAA Journal*, 58:2221–2235, 2020. ISSN 00011452. doi: 10.2514/1.J058744.

[28] S. Ashwin Renganathan, Yingjie Liu, and Dimitri N. Mavris. Koopman-based approach to nonintrusive projection-based reduced-order modeling with black-box high-fidelity models. *AIAA Journal*, 56:4087–4111, 2018. ISSN 00011452. doi: 10.2514/1.J056812.

[29] S. Ashwin Renganathan, Romit Maulik, and Vishwas Rao. Machine learning for nonintrusive model order reduction of the parametric inviscid transonic flow past an airfoil. *Physics of Fluids*, 32, 4 2020. ISSN 1070-6631. doi: 10.1063/1.5144661.

[30] S Ashwin Renganathan, Jeffrey Larson, and Stefan M Wild. Lookahead acquisition functions for finite-horizon time-dependent bayesian optimization and application to quantum optimal control. *arXiv preprint arXiv:2105.09824*, 2021.

[31] S Ashwin Renganathan, Romit Maulik, and Jai Ahuja. Enhanced data efficiency using deep neural networks and gaussian processes for aerodynamic design optimization. *Aerospace Science and Technology*, 111:106522, 2021.

[32] S Ashwin Renganathan, Vishwas Rao, and Ionel M Navon. Camera: A method for cost-aware, adaptive, multifidelity, efficient reliability analysis. *Journal of Computational Physics*, 472:111698, 2023.

[33] Sudharshan Ashwin Renganathan. A methodology for non-intrusive projection-based model reduction of expensive black-box pde-based systems and application in the many-query context. 2018.

[34] C. W. Rowley. Model reduction for fluids, using balanced proper orthogonal decomposition. *International Journal of Bifurcation and Chaos*, 15:997–1013, 11 2011. ISSN 02181274. doi: 10.1142/S0218127405012429.

[35] Clarence W. Rowley, Tim Colonius, and Richard M. Murray. Model reduction for compressible flows using pod and galerkin projection. *Physica D: Nonlinear Phenomena*, 189:115–129, 2 2004. ISSN 0167-2789. doi: 10.1016/j.physd.2003.10.017.

[36] V. V. Rusanov. The calculation of the interaction of non-stationary shock waves and obstacles. *USSR Computational Mathematics and Mathematical Physics*, 1:304–320, 1 1962. ISSN 0041-5553. doi: 10.1016/0041-5553(62)90062-9.

[37] Alvaro Sanchez-Gonzalez, Jonathan Godwin, Tobias Pfaff, Rex Ying, Jure Leskovec, and Peter W. Battaglia. Learning to simulate complex physics with graph networks. 2020. doi: 10.48550/arXiv.2002.09405.

[38] Peter J. Schmid. Dynamic mode decomposition of numerical and experimental data. *Journal of Fluid Mechanics*, 656:5–28, 2010. ISSN 1469-7645. doi: 10.1017/S0022112010001217.

[39] L. Sirovich. Turbulence and the dynamics of coherent structures. part I: Coherent structures. *Quarterly of Applied Mathematics*, 45(3):561–571, 1987. doi: 10.1090/qam/910462.

[40] Joseph L. Steger and R. F. Warming. Flux vector splitting of the inviscid gasdynamic equations with application to finite-difference methods. *Journal of Computational Physics*, 40:263–293, 4 1981. ISSN 0021-9991. doi: 10.1016/0021-9991(81)90210-2.

[41] Di Sun, Zirui Wang, Feng Qu, and Junqiang Bai. A deep learning based prediction approach for the supercritical airfoil at transonic speeds. *Physics of Fluids*, 33, 8 2021. ISSN 10897666. doi: 10.1063/5.0060604.

[42] Bram van Leer. Towards the ultimate conservative difference scheme. v. a second-order sequel to godunov’s method. *Journal of Computational Physics*, 32:101–136, 7 1979. ISSN 0021-9991. doi: 10.1016/0021-9991(79)90145-1.

[43] Pauli Virtanen, Ralf Gommers, Travis E Oliphant, Matt Haberland, Tyler Reddy, David Cournapeau, Evgeni Burovski, Pearu Peterson, Warren Weckesser, Jonathan Bright, et al. Scipy 1.0: fundamental algorithms for scientific computing in python. *Nature methods*, 17(3):261–272, 2020. doi: 10.1038/s41592-020-0772-5.

[44] Jincheng Wang, Haiyang Hu, Ping He, and Hui Hu. A machine learning study to predict wind-driven water runback characteristics. *Physics of Fluids*, 35, 10 2023. ISSN 10897666. doi: 10.1063/5.0167545.

[45] G. Welper. Interpolation of functions with parameter dependent jumps by transformed snapshots. *SIAM Journal on Scientific Computing*, 39:A1225–A1250, 7 2017. ISSN 10957197. doi: 10.1137/16M1059904.

[46] Xiangjie Yao, Rui Huang, and Haiyan Hu. Data-driven modeling of transonic unsteady flows and efficient analysis of fluid–structure stability. *Journal of Fluids and Structures*, 111, 5 2022. ISSN 10958622. doi: 10.1016/j.jfluidstructs.2022.103549.

[47] Ian T. Young and Lucas J. van Vliet. Recursive implementation of the gaussian filter. *Signal Processing*, 44(2):139–151, Jun 1995. doi: 10.1016/0165-1684(95)00020-E.

[48] Wei Wei Zhang and Bernd R. Noack. Artificial intelligence in fluid mechanics. *Acta Mechanica Sinica*, 37:1715–1717, 12 2021. ISSN 16143116. doi: 10.1007/s10409-021-01154-3.

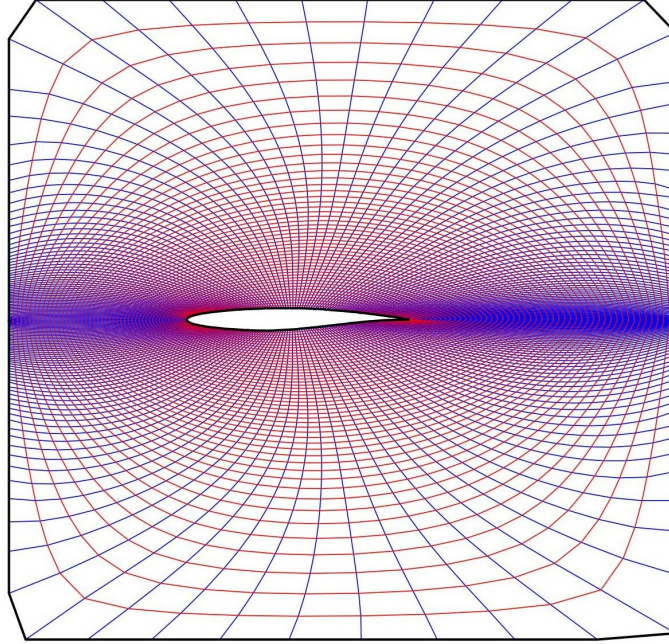


Figure 13: zoomed view of O-grid mesh

A Example of kernel matrix

To better understand this, consider a snapshot \mathbf{u} of $n = 5$ elements. Then, one can obtain the convolved output $\mathbf{u}^s = B\mathbf{u}$ in matrix form as;

$$\begin{pmatrix} \mathbf{u}^s[0] \\ \mathbf{u}^s[1] \\ \mathbf{u}^s[2] \\ \mathbf{u}^s[3] \\ \mathbf{u}^s[4] \end{pmatrix} = \begin{pmatrix} \mathbf{k}[2] & \mathbf{k}[1] + \mathbf{k}[3] & \mathbf{k}[0] + \mathbf{k}[4] & 0 & 0 \\ \mathbf{k}[1] & \mathbf{k}[0] + \mathbf{k}[2] & \mathbf{k}[3] & \mathbf{k}[4] & 0 \\ \mathbf{k}[0] & \mathbf{k}[1] & \mathbf{k}[2] & \mathbf{k}[3] & \mathbf{k}[4] \\ 0 & \mathbf{k}[0] & \mathbf{k}[1] & \mathbf{k}[2] + \mathbf{k}[4] & \mathbf{k}[3] \\ 0 & 0 & \mathbf{k}[0] + \mathbf{k}[4] & \mathbf{k}[1] + \mathbf{k}[3] & \mathbf{k}[2] \end{pmatrix} \cdot \begin{pmatrix} \mathbf{u}[0] \\ \mathbf{u}[1] \\ \mathbf{u}[2] \\ \mathbf{u}[3] \\ \mathbf{u}[4] \end{pmatrix} \quad (22)$$

The main idea is to convolve the given snapshot data matrix U , construct ROM for the convolved (smoothed) snapshots \mathbf{u}^s and invert the predicted convolved snapshot to obtain the unsmoothed prediction.